Research Article Vol. 30, No. 2 / 17 Jan 2022 / *Optics Express* 1584

Optics EXPRESS

High-power terahertz pulse generation from bias-free nanoantennas on graded composition InGaAs structures

PING-KENG LU,[1,2] **DENIZ TURAN,**[1,2] **AND MONA JARRAHI**[1,2,*]

[1] *Electrical and Computer Engineering Department, University of California, Los Angeles, CA 90095, USA*
[2] *California NanoSystems Institute, University of California, Los Angeles, CA 90095, USA*
[*] *mjarrahi@ucla.edu*

Abstract: We present a bias-free photoconductive emitter that uses an array of nanoantennas on an InGaAs layer with a linearly graded Indium composition. The graded InGaAs structure creates a built-in electric field that extends through the entire photoconductive active region, enabling the efficient drift of the photo-generated electrons to the nanoantennas. The nanoantenna geometry is chosen so that surface plasmon waves are excited in response to a 1550 nm optical pump to maximize photo-generated carrier concentration near the nanoantennas, where the built-in electric field strength is maximized. With the combination of the plasmonic enhancement and built-in electric field, high-power terahertz pulses are generated without using any external bias voltage. We demonstrate the generation of terahertz pulses with 860 µW average power at an average optical pump power of 900 mW, exhibiting the highest radiation power compared to previously demonstrated telecommunication-compatible terahertz pulse emitters.

1. Introduction

Photoconductive antennas are one of the most widely used terahertz emitters, enabling the generation of both broadband and narrowband terahertz radiation through a compact, cost-effective, and room temperature platform [1–23]. A key design aspect of these terahertz emitters is to provide a large enough electric field within the photoconductive active region, where upon optical excitation, the photo-generated charge carriers are accelerated and swept into the antenna electrodes to radiate terahertz waves. This electric field is usually provided by an external bias voltage that is applied across the antenna terminals. The requirement for an external bias voltage leads to serious challenges especially when using photoconductive substrates with low dark resistivity. For example, to develop telecommunication-compatible photoconductive terahertz emitters pumped with compact and low-cost fiber lasers at ~1550 nm wavelength range, photoconductive substrates with small bandgap energy (e.g. InGaAs) are required, which have low dark resistivity [24–26]. The low dark resistivity results in excessive dark current levels under an external bias voltage, which ultimately results in early thermal breakdown. During the past decade, several short-carrier-lifetime semiconductor structures have been developed to offer ultrafast photoconductive response while maintaining a dark resistivity above 1000 Ω.cm [27–30]. However, the developed telecommunication-compatible photoconductive terahertz emitters based on these engineered semiconductor structures require fairly high bias voltages (> 120 V) to achieve large enough (> 45 µW) terahertz power levels [28–33].

We recently demonstrated an alternative approach to develop high-efficiency photoconductive terahertz emitters without requiring any external bias voltage, leading to a complete elimination of the dark current. Instead of using an external bias voltage, we utilized the naturally-induced built-in electric field by the Fermi level pinning at the surface of an InAs substrate [34]. In particular, by growing a 500-nm-thick p+ InAs layer followed by a 100-nm-thick undoped InAs layer on a semi-insulating GaAs substrate (undoped InAs emitter), a strong band bending was

#447733 https://doi.org/10.1364/OE.447733
Journal © 2022 Received 4 Nov 2021; revised 21 Dec 2021; accepted 21 Dec 2021; published 5 Jan 2022

created at the surface of the undoped InAs layer for accelerating the photo-generated carriers. In addition, with a plasmonic nanoantenna array designed to maximize the near field optical generation at 1550 nm around each nanoantenna element, the carrier transport distances were greatly reduced to further enhance optical-to-terahertz conversion efficiency [35–47]. Through this undoped InAs emitter design, passive optical-to-terahertz conversion was demonstrated with efficiencies exceeding other passive terahertz emitters based on nonlinear optical processes (by 4 orders of magnitude) [48,49], photo-Dember effect [50,51], and spintronics [52,53]. Here we present a bias-free photoconductive emitter based on an InGaAs photo-absorbing layer with a linearly graded Indium composition (graded InGaAs emitter). The use of the graded InGaAs layer extends the built-in electric field through the entire InGaAs layer to drift almost all of the photo-generated carriers to the terahertz radiating elements, leading to the generation of terahertz pulses with ~4 times higher total radiation power while introducing a slight reduction in bandwidth compared to the undoped InAs emitter. A detailed quantitative analysis is performed to describe and compare the two emitter structures in terms of their carrier dynamics and radiation properties, which is supported by the experimental results. The high radiation power, broad bandwidth, telecommunication compatibility, bias-free and reliable operation of the presented graded InGaAs emitter extend the scope and potential uses of terahertz pulse emitters to practical imaging and sensing applications.

2. Device design and analysis

2.1. Device operation principle

Schematic diagram and operation principles of the graded InGaAs emitter are illustrated in Fig. 1. A nanoantenna array is fabricated on a 500-nm-thick, 1.4×10^{19} cm^{-3} Be-doped InGaAs layer grown on a semi-insulating GaAs substrate. The InGaAs layer has a linearly graded Indium composition varying from 60% at the InGaAs/GaAs interface to 100% at the surface. With the valence band (VB) flattened out due to the p+ doping, the graded bandgap creates a slope in the conduction band (CB), which induces a built-in electric field that drifts the photo-generated electrons toward the nanoantenna electrodes at the surface. The geometry of the nanoantennas is chosen to enhance optical intensity near the nanoantennas, where the built-in field strength is maximized, by the excitation of surface plasmon waves. In order to excite surface plasmon waves at ~1550 nm wavelength range, the nanoantennas are designed in the form of gratings with a 440 nm periodicity, 80 nm gap, and 80 nm metal height, covered by a 240-nm-thick Si_3N_4 anti-reflection coating.

To examine the impact of the Indium composition gradient on the carrier transport, Fig. 2 shows the energy band diagrams and CB quasi-electric field profiles of graded InGaAs structures with different starting compositions at the InGaAs/GaAs interface, calculated using a semiconductor device simulator (Sentaurus). It should be noted that the electric force in a semiconductor heterostructure is not only determined by the electric field, but also by the gradient of the electron affinity χ_s and bandgap energy E_g. Therefore, the quasi-electric fields are defined for the CB and VB separately as,

$$F_e = -\frac{dE_c}{dx} = q\frac{dV}{dx} + \frac{d\chi_s}{dx} = -q\mathcal{E}_c^*, \tag{1}$$

$$F_h = \frac{dE_v}{dx} = -q\frac{dV}{dx} - \frac{d(\chi_s + E_g)}{dx} = q\mathcal{E}_v^*, \tag{2}$$

where $F_e,\ F_h$ are the electric forces exerted on electrons and holes, $E_c,\ E_v$ are the CB and VB energies, V is the electrostatic potential, and $\mathcal{E}_c^*,\ \mathcal{E}_v^*$ are the quasi-electric fields for the CB and VB, respectively. Generally, the quasi-electric fields for the CB and VB can be different. As clearly shown in Fig. 2, the p+ graded InGaAs structure has a non-zero CB quasi-electric field, which depends on the starting Indium composition at the InGaAs/GaAs interface, while the VB

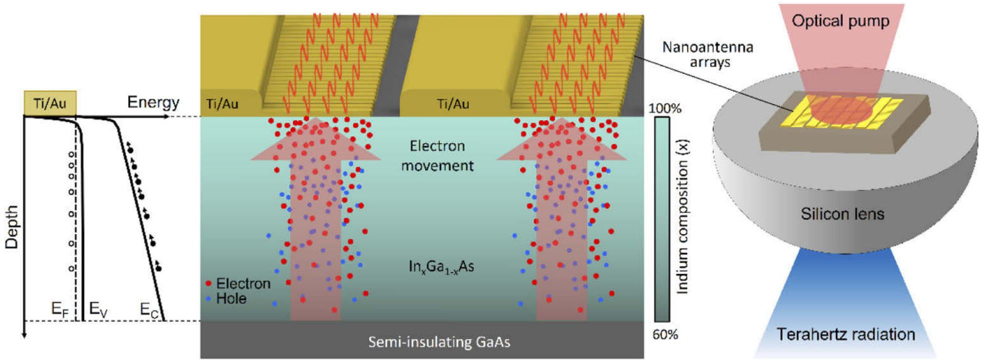

Fig. 1. Schematic diagram and operation principles of the graded InGaAs emitter, illustrating the electron movement within the epitaxial graded InGaAs layer toward the nanoantenna array at the surface. Energy band diagram of the graded InGaAs layer is shown on the left, where the Fermi, conduction band minimum, and valence band maximum energy levels are marked as E_F, E_c, and E_v, respectively.

quasi-electric field is almost zero except for a ~20 nm depth near the surface. For the starting Indium composition of 60%, the CB quasi-electric field is ~ 6 kV/cm throughout nearly the entire epitaxial structure, which leads to a steady-state drift velocity of ~ 1.5×10^7 cm/s [54–62] (see Appendix A for more details). Higher composition gradients could potentially lead to stronger built-in quasi-electric fields, but the material quality could be severely degraded by the additional dislocation defects caused by the larger strain in the lattice [63–65]. Therefore, the starting Indium composition of 60% is chosen for the epitaxial growth. As shown in Fig. 2, for the pure p+ InAs structure without any bandgap gradient, the CB quasi-electric field decays rapidly into the substrate, and therefore it will accelerate only a small fraction of the photo-generated electrons within the top 10-20 nm.

To compare the graded InGaAs emitter with the undoped InAs emitter, Fig. 3 shows both of their energy band diagrams and CB quasi-electric field profiles. In contrast to the graded InGaAs structure with its CB quasi-electric field extending throughout the entire photo-absorbing semiconductor region, the undoped InAs structure has a much stronger field (> 30 kV/cm) which is concentrated within a shallower depth of 100 nm. Importantly, within such a small carrier transport range with minimal defects under a high accelerating field, where scattering events are almost negligible, most of the photo-generated electrons would transport quasi-ballistically. To justify this, we consider the electron mobility in the undoped InAs layer to be 10^4 cm^2/V/s [66] and the scattering time in bulk InAs to be ~130 fs at room temperature [67]. This scattering time is larger than the ballistic transit time for electrons over the 100-nm-thick undoped InAs layer under the uniform field intensity of 30 kV/cm, which is calculated to be 93 fs [68],

$$\tau_{tr} = \sqrt{2m^* L / q\mathcal{E}_c^*}, \tag{3}$$

where m^* is the effective mass of electron in bulk InAs and L is the transport distance. As a result, compared to the graded InGaAs structure, the undoped structure is expected to collect less electrons but with a much higher velocity than the electron saturation velocity, an effect usually termed "velocity overshoot" [69,70]. After being accelerated for τ_{tr}, the final electron ballistic velocity can be obtained by [68]

$$v_{bal} = q\mathcal{E}_c^* \tau_{tr} / m^*, \tag{4}$$

which is the theoretical upper limit of the electron velocity with absolutely no scattering events. To consider all electrons generated at different depths in the substrate, we calculate the

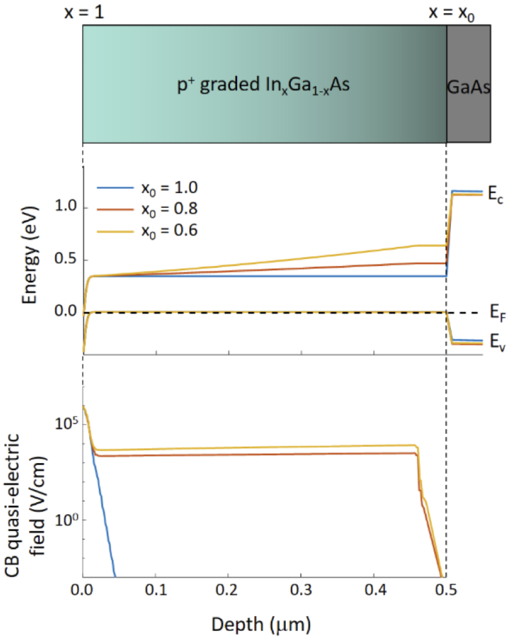

Fig. 2. Energy band diagram and CB quasi-electric field of the graded InGaAs semiconductor structure for different starting Indium compositions at the InGaAs/GaAs interface.

weighted average of ballistic velocities using the simulated optical generation profile under the nanoantennas, and obtain 1.3×10^8 cm/s as the theoretical upper limit of the average electron velocity. In reality, a few scattering events could still occur during the transport in addition to the carrier screening that could further reduce the CB quasi-electric field, leading to lower electron velocities. On the other hand, the graded InGaAs structure has much longer carrier transit times compared with the scattering time in InGaAs due to its deeper CB quasi-electric field extension and the high p+ doping. This suggests that the electron drift velocity will reach its steady-state value within a small fraction of the total transit time. Therefore, we assume that the electrons travel non-ballistically at a steady-state drift velocity of ~ 1.5×10^7 cm/s [54–62].

2.2. Photoconductive impulse response calculation

An in-depth analysis is performed to calculate the impulse responses of these two substrate structures under a 1550 nm optical excitation to theoretically investigate radiation characteristics of the graded InGaAs and undoped InAs emitters. We solve the drift-diffusion equation for electrons to obtain the transient electron concentrations over the photoconductive active regions of both semiconductor structures. Since the built-in electric field is normal to the substrate surface, electron movements parallel to the surface are not considered below. Denoting + y axis as the direction into the substrate with y = 0 at the surface, we have

$$\frac{\partial n}{\partial t} = \frac{\partial (v_e n)}{\partial y} + D_n \frac{\partial^2 n}{\partial y^2} - \frac{n}{\tau_e}, \tag{5}$$

$$n(y,\ 0) = G_0(y), \tag{6}$$

where $n = n(y,\ t)$ is the electron concentration as a function of position y and time t, v_e is the electron drift velocity, D_n is the electron diffusion constant, τ_e is the electron minority carrier lifetime, and $G_0(y)$ is the optical generation profile, obtained by numerical simulations

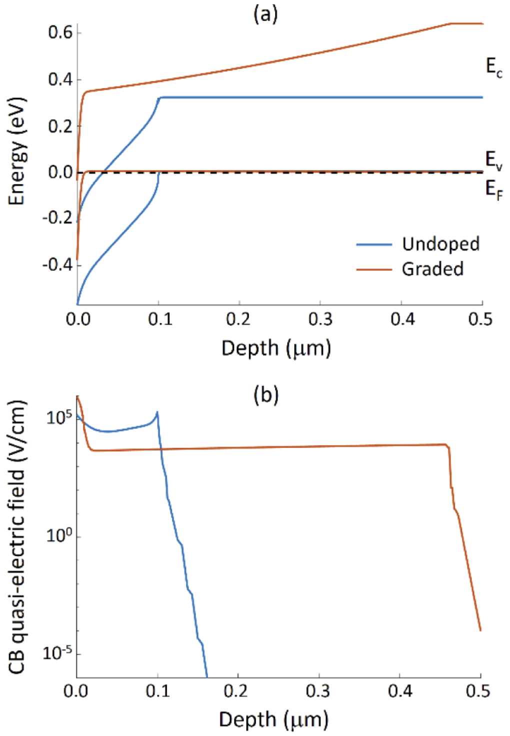

Fig. 3. (a) Energy band diagram and (b) CB quasi-electric field of the undoped InAs and graded InGaAs semiconductor structures, where the undoped InAs structure is composed of a 500-nm-thick, 1.4×10^{19} cm^{-3} Be-doped InAs layer followed by a 100-nm-thick undoped InAs layer on a semi-insulating GaAs substrate and the graded InGaAs structure is composed of a 500-nm-thick, 1.4×10^{19} cm^{-3} Be-doped InGaAs layer on a semi-insulating GaAs substrate.

(Fig. 4(a)). The electron recombination lifetime of the 1.4×10^{19} cm^{-3} Be-doped InAs substrate is experimentally measured to be ~5 ps [34]. Considering the electron diffusion coefficient of $D_n = 1.3 \times 10^{-3}\ m^2/s$ [66,71], the diffusion term is estimated to be much smaller than the drift term in the undoped InAs region and recombination terms in the p+ regions of both devices (see more detail in Appendix B). Therefore, the diffusion term is ignored and the transient electron concentration values are calculated analytically.

For the graded InGaAs structure, considering $v_e = 1.5 \times 10^7\ cm/s$ and $\tau_e = 5\ ps$, the transient electron concentration values are calculated as,

$$n(y,\ t) = G_0(y + v_e t)e^{-t/\tau_e}. \tag{7}$$

This solution is in the form of a decaying traveling wave in the -y direction toward the electrodes with a speed of v_e. This traveling wave form of solution describes the electron drift under a uniform electric field with an exponential decay due to the electron recombination occurring at the same time.

For the undoped InAs structure, the electron velocity is modeled as a logistic function of y to take into account the sharp change in velocity between the undoped and doped regions. By considering $\tau_e = 5\ ps$, the solution is

$$n(y,\ t) = \frac{G_0\left(f^{-1}\left(y + v_{bal}t + \frac{1}{k}e^{k(y-w)}\right)\right) \cdot v_e\left(f^{-1}\left(y + v_{bal}t + \frac{1}{k}e^{k(y-w)}\right)\right) \cdot e^{-t/\tau_e}}{v_e(y)}, \tag{8}$$

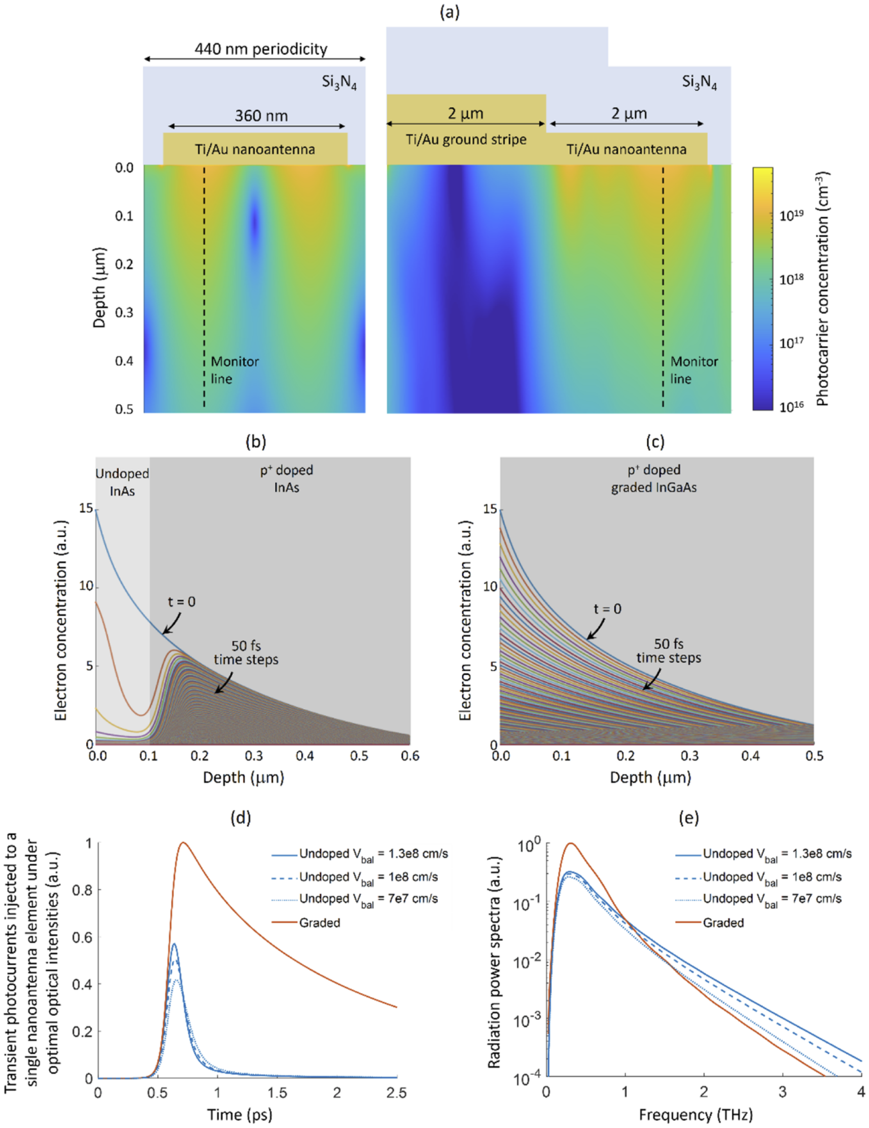

Fig. 4. (a) Peak photocarrier concentration generated within the photoconductive active region at an average optical power of 900 mW (assuming a 120 fs pulsewidth and a 76 MHz repetition rate) calculated using a finite-difference-time-domain-based electromagnetic solver (Lumerical). Cross-sections perpendicular to (left) and in parallel with (right) the nanoantenna orientation are shown, where the dashed monitor lines show the position with the highest photocarrier concentration. (b) Calculated impulse response of electron concentration for the undoped InAs emitter with a 50 fs time resolution, assuming $v_{bal} = 1.3 \times 10^8\ cm/s$. (c) Calculated impulse response of electron concentration for the graded InGaAs emitter with a 50 fs time resolution. (d) Calculated transient photocurrents injected to a single nanoantenna element for the undoped InAs emitter (under various ballistic velocities) and graded InGaAs emitter for a laser pulsewidth of 120 fs. (e) Calculated power spectra generated by the entire nanoantenna arrays of the undoped InAs and graded InGaAs emitters.

where v_{bal} is the average ballistic velocity in the undoped region, $w = 100\ nm$ is the depth of the undoped region, k is the factor that controls the sharpness of the velocity drop, which is taken to be 0.1 nm^{-1}, $v_e(y) = v_{bal}/(1 + e^{k(y-w)})$, and $f(y) = y + e^{k(y-w)}/k$. The solution converges to the same form as for the graded InGaAs structure when y is within the undoped region far enough from the undoped/p+ interface,

$$n(y,\ t)\ \sim\ G_0(y + v_{bal}t)e^{-t/\tau_e},\ for\ y \ll w. \tag{9}$$

Figures 4(b) and 4(c) show the time evolution of the electron concentration solutions under the same incident optical intensities for the undoped InAs (assuming $v_{bal} = 1.3 \times 10^8\ cm/s$) and graded InGaAs semiconductor structures with a time resolution of 50 fs at the depth cross section with the highest optical generation (monitor lines shown in Fig. 4(a)). Under higher quasi-electric field and ballistic transport, the electrons in the undoped region of the undoped InAs structure are rapidly swept out to the nanoantenna electrodes, leaving the rest of the electrons in the p+ region to be recombined with a lifetime of 5 ps. The dramatic behavior changes from undoped to p+ doped region is clearly observed in Fig. 4(b). In contrast, the graded InGaAs structure (Fig. 4(c)) shows a smooth reduction of electron concentration caused by both the drift current and carrier recombination. Moreover, it can be seen that the deeper electrons are collected more effectively compared to the undoped InAs structure due to the CB quasi-electric field extending over almost the entire InGaAs layer, suggesting an increase in the low frequency radiation components.

Using the calculated impulse response of electron concentration, the impulse response of the injected photocurrent to the nanoantennas fabricated on the undoped InAs and graded InGaAs semiconductor structures is calculated. Since both structures are terminated with a high-conductivity InAs layer (with surface Fermi level pinning above the conduction band), the nanoantenna metal - InAs junctions are expected to have very low contact resistance and negligible energy barrier for electrons (Ohmic contact). An important difference between the undoped InAs and graded InGaAs emitters is their experimentally observed optimal optical beam sizes (1/e^2 beam diameter of 330 µm and 100 µm for the undoped InAs emitter and graded InGaAs emitter, respectively) at which they provide the highest radiation power. This difference is attributed to weaker carrier screening in the graded InGaAs emitter due to its flat valence band, leading to negligible hole accumulation within the active region. Carrier screening of the electric field originates from the presence of high carrier concentrations, which create an opposing electric field that consequently reduces the acceleration of the carriers and the radiation power. Different optical beam sizes translate to different incident optical intensity levels under the same optical power. Figure 4(d) shows the transient photocurrents injected to a single antenna element at the optimum optical intensity for both emitters calculated by convolving the impulse response photocurrents with the temporal profile of a 120 fs sech^2-shaped laser pulse used for the experimental characterization. The calculated transient photocurrents for the undoped InAs structure are plotted for different ballistic velocities because screening of the built-in electric field as a result of the photocarrier drift as well as a small number of scattering events could lower the actual electron velocity in the undoped InAs structure. Higher ballistic velocity in the undoped InAs structure leads to sharper transient response, which in the frequency-domain translates to a slower frequency roll-off (Fig. 4(e)). Figure 4(e) shows the estimated power spectra generated by the two emitters obtained by calculating the emitted radiation from the entire nanoantenna array (see more detail in Appendix C). Compared to the undoped InAs structure, the large photocurrent decay time of the graded InGaAs structure provides stronger sub-terahertz radiation power at a cost of slightly faster frequency roll-off since electrons generated deeper in the InGaAs layer drift to the nanoantennas. The results of this quantitative analysis agree very well with the experimental results discussed in the next section.

3. Experimental results and discussion

Emitters with the same nanoantenna geometry as described in [34] and a total active area of 1 × 1 mm^2 are fabricated on the graded InGaAs semiconductor structures grown through molecular beam epitaxy. Each nanoantenna element has a length of 2 µm to maintain a high-efficiency and broadband radiation performance [34]. The ground stripes have a 2 µm width and a 0.5 µm gap size from the adjacent nanoantenna tips. Fabrication of the emitter prototypes starts with electron beam lithography and Ti/Au deposition to form the nanoantenna array as well as the ground stripes sequentially. The 240-nm-thick Si_3N_4 anti-reflection coating is deposited next through plasma-enhanced chemical vapor deposition. Figure 5(a) shows the optical and scanning electron microscopy images of a graded InGaAs emitter prototype.

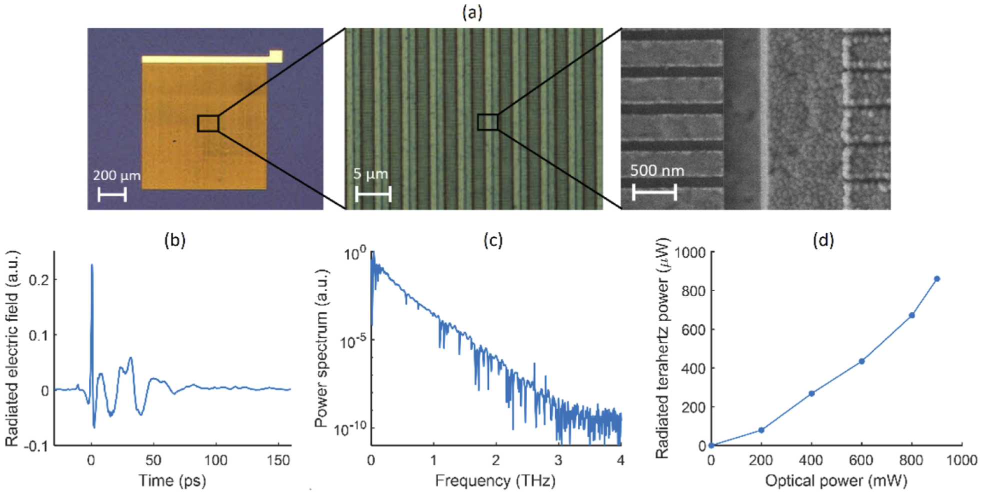

Fig. 5. (a) Optical and scanning electron microscopy images of a fabricated graded InGaAs emitter prototype. (b) The measured terahertz time-domain electric field, (c) radiated power spectrum, and (d) total radiated power of the graded InGaAs emitter prototype. (b) and (c) are measured under an average optical power of 450 mW.

A graded InGaAs emitter prototype is mounted on a hyper-hemispherical silicon lens to better collimate the generated terahertz radiation. The radiated power spectrum of the emitter is characterized using a terahertz time-domain spectroscopy system, where an optical parametric oscillator pumped by a Ti:Sapphire laser (Coherent Mira HP) generates femtosecond pulses at a 76 MHz repetition rate, with a 120 fs pulse-width and a center wavelength of ~ 1550 nm. A beam splitter separates the optical beam into two branches for the excitation of the emitter and an H-dipole-based PCA detector fabricated on an ErAs:InGaAs substrate [23]. While changing the time delay between the two branches, the detector output photocurrent is amplified using a transimpedance amplifier (FEMTO DHPCA at 10^6 V/A gain) and recorded, signifying the time-domain terahertz waveform, as shown in Fig. 5(b). Since the radiated electric field is proportional to the time derivative of the transient photocurrent, the negative cycle of the sub-picosecond terahertz pulses radiated by the graded InGaAs emitter is significantly lower than the positive cycle due to the long photocurrent decay time predicted in Fig. 4(d). Through Fourier transform of the time-domain waveform, the radiated power spectrum is obtained (Fig. 5(c)), showing a radiation bandwidth larger than 3 THz when capturing and averaging only 10 traces over a 5 second data acquisition time. It should be noted that the H-dipole-based PCA detector used for our measurements exhibits a resonant behavior at low frequencies, which results in ringing in the detected spectrum. The low frequency resonances are also observed in the measured time-domain electric field. The broad bandwidth of the generated radiation is due to the sub-picosecond rising edge of the generated pulses, which provides high frequency radiation components.

The total radiated power from the emitter is measured using a calibrated pyroelectric detector (Sensors und Lasertechnik THz-30 detector calibrated by Physikalisch-Technische Bundesanstalt, Germany). Terahertz pulses with 860 µW average power are generated at an average optical pump power of 900 mW, exhibiting ~4 times higher radiation power compared to the undoped InAs emitter [34], which is in agreement with the theoretical predictions shown in Fig. 4(e). This is the highest reported radiation power compared with the previously demonstrated telecommunication-compatible photoconductive terahertz pulse emitters [28–33]. The radiation power of the graded InGaAs emitter increases super-linearly as a function of the optical pump power with no signs of saturation, suggesting even higher radiation power and efficiency at higher optical pump powers. While the dominant radiation mechanism relies on the electron drift current feeding the nanoantennas, there could be other secondary mechanisms such as photo-Dember effect and nonlinear optical processes contributing to the generated terahertz power.

As mentioned earlier, the optimal diameter of the optical beam incident on the graded InGaAs emitter under pulsed operation is experimentally determined to be ∼100 µm. To further investigate the impact of the optical beam size, we characterize the emitter when generating quasi-continuous wave (CW) terahertz radiation at different frequencies as a function of the optical excitation intensity. The optical beam from two C-band CW lasers (Santec 510 and QPhotonics QDFBLD-1550-10) are combined in a fiber and pulse-modulated at a 1 MHz frequency with a 10% duty cycle using an acousto-optic modulator (Gooch & Housego R15200-.2-1.55-GaP-FO-GH). The modulated beam is then amplified to an average optical power of 300 mW using an Erbium-doped fiber amplifier (HPFA-C-33-IA). Photomixing of the two beams induces an oscillating photocurrent on the nanoantennas at the difference frequency of the two beams, which is tunable by varying the wavelength of one of the CW seed lasers. The radiated power is measured using a superconducting bolometer (QMC Instruments Ltd. Model QNbB/PTC). At the same total optical power level, the optical beam size incident on the nanoantenna array is adjusted to vary the optical excitation intensity. Figure 6 shows the measured radiation power at different terahertz frequencies as a function of the $1/e^2$ optical beam diameter. An optimal optical beam size that maximizes the radiated power is clearly observed at each terahertz frequency. At very small beam sizes, the carrier screening becomes too strong, creating an opposing electric field that consequently reduces the acceleration of the carriers and the radiation power. On the other hand, at very large beam sizes, the destructive interference of the radiation from the nanoantennas decreases the total radiated power. This is clearly revealed by the fact that the optimal beam diameter decreases as the terahertz frequency increases, where the destructive interference gets stronger at shorter wavelengths. Finally, it should be noted that the optimal beam diameter values

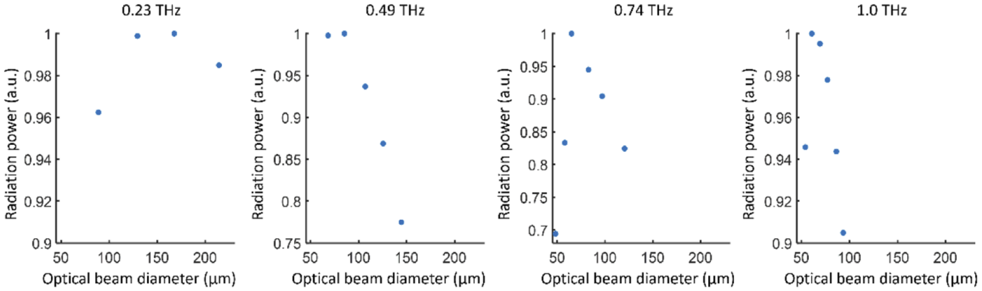

Fig. 6. Measured quasi-CW radiation power from the graded InGaAs emitter as a function of the $1/e^2$ incident optical beam diameter at various terahertz frequencies.

shown in Fig. 6 support the optimal value of ~ 100 µm under pulsed operation, which contains the contribution from all of the radiated frequency components.

4. Conclusion

In summary, we demonstrate high-power terahertz pulse generation from bias-free nanoantennas on a graded composition InGaAs structure with a linearly graded Indium composition. Such a semiconductor heterostructure creates a deep built-in quasi-electric field that extends throughout the entire thickness of the InGaAs layer while maintaining a field strength that is high enough to drift the photo-generated electrons at high velocities. As a result, the number of the collected electrons by the nanoantennas that contribute to terahertz pulse generation is increased. Furthermore, by the excitation of surface plasmon waves along the nanoantennas at ~1550 nm wavelength range, the optical generation is significantly enhanced within a few hundred nanometers beneath each nanoantenna element, where the built-in electric field strength is maximized, greatly reducing the transit time of the photo-generated electrons to the radiating nanoantennas. Using a fabricated graded InGaAs emitter, we demonstrate the generation of terahertz pulses with a record-high 860 µW average power at an average optical pump power of 900 mW. It should be pointed out that further optimization of the layer thicknesses, composition gradient, and doping levels could provide even faster carrier dynamics to increase the radiation power and bandwidth of the bias-free photoconductive emitters beyond the prototypes explored in this work. In addition, a distributed Bragg reflector at the bottom of the photoconductive structure could form an optical cavity to further enhance the power efficiencies [43]. The high radiation power and high reliability of the presented terahertz emitter, without requiring any external bias voltage or special optical focus and alignment requirements, would be very attractive for real-world terahertz imaging and spectroscopy systems. As previously demonstrated [34], the emitter chip can be simply mounted at the tip of an optical fiber to provide a flexible platform for diverse application scenarios.

Appendix A: Steady-state electron drift velocity in the graded InGaAs structure

The electron drift velocity is quantified by the following empirical formula [56],

$$v_e = \frac{\mu_e \mathcal{E}}{\sqrt{1 + \left(\frac{\mu_e \mathcal{E}}{v_{sat}}\right)^2}}, \tag{10}$$

where v_e is the electron drift velocity, μ_e is the low-field electron mobility, $\mathcal{E}$ is the electric field, and $v_{sat} = \sqrt{2E_{phonon}/m^*}$ is the approximated saturation velocity determined by the optical phonon energy E_{phonon} and effective mass m^*. The low-field mobility values, effective masses, and optical phonon energies for highly doped $\mathrm{In_{0.53}Ga_{0.47}As}$ and InAs are found from the literature [57–62]. Using these parameters, for an electric field of 6 kV/cm in the graded InGaAs emitter, similar velocities of ~ 1.5×10^7 cm/s are obtained for both $\mathrm{In_{0.53}Ga_{0.47}As}$ and InAs. This justifies that the approximation of a constant steady-state drift velocity of 1.5×10^7 cm/s throughout the entire graded InGaAs structure is valid.

Appendix B: Estimation of the diffusion term for impulse response calculation

To see why the diffusion current can be ignored in the closed form calculations, it should be noted that the initial carrier concentration is determined by the plasmonic-enhanced optical generation profile, which follows an exponential decay into the substrate due to the evanescent nature of the surface plasmon waves. In other words, the initial carrier concentration can be approximated as $n_0 e^{-y/L_0}$, where n_0 denotes the initial electron concentration at the surface and $L_0 \sim 210\ nm$

characterizes the decay rate of the electron concentration into the substrate. Therefore, the diffusion current is approximately

$$J_{diff} = \frac{D_n}{L_0^2} n_0 e^{-y/L_0}, \tag{11}$$

while the drift term J_{drift} and recombination term R are

$$J_{drift} = \frac{v_e}{L_0} n_0 e^{-y/L_0}, \tag{12}$$

$$R = \frac{-1}{\tau_e} n_0 e^{-y/L_0}. \tag{13}$$

Comparing the constant factors of the three terms with $L_0 = 210\ nm$, $D_n = 1.3 \times 10^{-3}\ m^2/s$, $v_e = 1.5 \times 10^7\ cm/s$ and $\tau_e = 5\ ps$, we have

$$\frac{D_n}{L_0^2} \ll \frac{v_e}{L_0}, \frac{D_n}{L_0^2} \ll \frac{1}{\tau_e}. \tag{14}$$

This justifies the negligible impact of the diffusion current. Similar arguments apply to the undoped InAs emitter due to its high quasi-ballistic velocity in the undoped region and 5 ps carrier lifetime in the p+ doped region. To further support this claim, the electron drift-diffusion equation is numerically solved for the graded InGaAs emitter with and without the diffusion term, showing a negligible difference between the two results that are shown in Fig. 7.

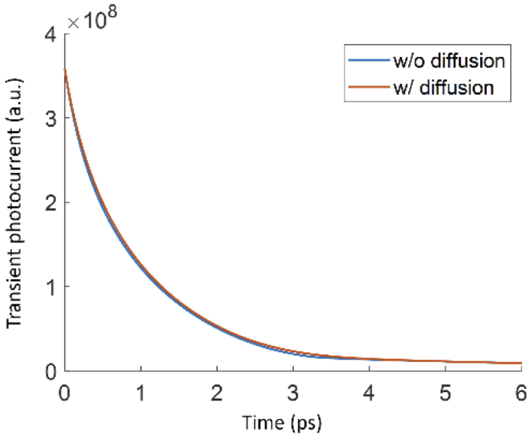

Fig. 7. Photocurrent impulse response obtained by numerically solving the electron drift-diffusion equation with and without the diffusion term.

Appendix C: Estimation of the radiated terahertz power spectrum

Due to the high conductivity of the substrates, a fraction of the injected currents (Fig. 4(d)) is directed to flow on the nanoantennas. The induced current on the nanoantennas is calculated by considering the antenna and substrate impedance levels. Next, the transient current induced on the nanoantennas is converted to the frequency domain, $I_{induced}(f)$, to obtain the radiated electric field $E_i(r,\ \theta,\ \phi,\ f)$ from a single nanoantenna element

$$E_i(r,\ \theta,\ \phi,\ f) \sim\ jksin\theta\frac{e^{-jkr}}{r}I_{induced}(f), \tag{15}$$

where $k = 2\pi fn/c$ is the wavevector, with n = 3.6 as the refractive index of GaAs. $(r,\ \theta,\ \phi)$ are the spherical coordinates with their orientations relative to the nanoantenna array illustrated in Fig. 8.

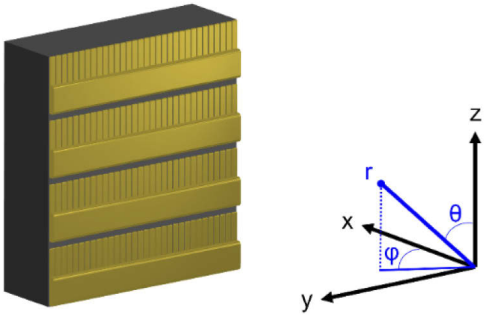

Fig. 8. Nanoantenna array orientation and the definition of the spherical coordinates.

Then, the far-field radiated power spectrum from the two-dimensional nanoantenna array excited by the incident optical beam is calculated using the nanoantenna array factors.

$$E_{array}(r, \theta, \phi, f) = E_i(r, \theta, \phi, f)AF_y(\theta, \phi, f)AF_z(\theta, f), \tag{16}$$

where AF_y and AF_z are the array factors of the nanoantenna array in the y and z directions:

$$AF_y(\theta, \phi, f) = \frac{sin\left(\frac{N_y\psi_y}{2}\right)}{sin\left(\frac{\psi_y}{2}\right)}, \psi_y = p_yksin\phi sin\theta, \tag{17}$$

$$AF_z(\theta, f) = \frac{sin\left(\frac{N_z\psi_z}{2}\right)}{sin\left(\frac{\psi_z}{2}\right)}, \psi_z = p_zkcos\theta, \tag{18}$$

where $p_y = 440$ nm and $p_z = 4.5$ µm are the periodicity of the nanoantennas in the y and z directions, respectively, and N_y and N_z are the number of nanoantennas in the y and z directions, respectively, determined by the incident optical beam size. Then, the total radiated power is obtained from the integral below.

$$P_{rad}(f) = \frac{1}{2\eta_0}\int_{-\pi/2}^{\pi/2}\int_{0}^{\pi}|E_{array}(\theta, \phi, f)|^2r^2sin\theta d\theta d\phi, \tag{19}$$

where η_0 is the vacuum wave impedance.

Funding. This work was supported by the Office of Naval Research (N000141912052) and Burroughs Wellcome Fund. Deniz Turan was supported by the U.S. Department of Energy (DE-SC0016925).

Acknowledgments. We acknowledge contributions of Dr. Baolai Liang from California NanoSystems Institute for the MBE growth of the substrates.

Disclosures. The authors declare no conflict of interest.

Data availability. Data underlying the results presented in this paper are not publicly available at this time but may be obtained from the authors upon reasonable request

References

1. D. H. Auston, K. P. Cheung, and P. R. Smith, "Picosecond photoconducting Hertzian dipoles," Appl. Phys. Lett. **45**(3), 284–286 (1984).
2. S. Verghese, K. A. McIntosh, S. Calawa, W. F. Dinatale, E. K. Duerr, and K. A. Molvar, "Generation and detection of coherent terahertz waves using two photomixers," Appl. Phys. Lett. **73**(26), 3824–3826 (1998).
3. P. U. Jepsen, R. H. Jacobsen, and S. R. Keiding, "Generation and detection of terahertz pulses from biased semiconductor antennas," J. Opt. Soc. Am. B **13**(11), 2424–2436 (1996).
4. G. Zhao, R. N. Schouten, N. Van Der Valk, W. Th Wenckebach, and P. C. M. Planken, "Design and performance of a THz emission and detection setup based on a semi-insulating GaAs emitter," Rev. Sci. Instrum. **73**(4), 1715–1719 (2002).
5. S. Matsuura, M. Tani, and K. Sakai, "Generation of coherent terahertz radiation by photomixing in dipole photoconductive antennas," Appl. Phys. Lett. **70**(5), 559–561 (1997).
6. M. Jarrahi and T. H. Lee, "High-power tunable terahertz generation based on photoconductive antenna arrays," in *2008 IEEE MTT-S Int. Microwave Symp. Digest* (2008), pp. 391–394.
7. E. Peytavit, S. Lepilliet, F. Hindle, C. Coinon, T. Akalin, G. Ducournau, G. Mouret, and J.-F. Lampin, "Milliwatt-level output power in the sub-terahertz range generated by photomixing in a GaAs photoconductor," Appl. Phys. Lett. **99**(22), 223508 (2011).
8. H. Roehle, R. J. B. Dietz, H. J. Hensel, J. Böttcher, H. Künzel, D. Stanze, M. Schell, and B. Sartorius, "Next generation 1.5 µm terahertz antennas: mesa-structuring of InGaAs/InAlAs photoconductive layers," Opt. Express **18**(3), 2296–2301 (2010).
9. Z. D. Taylor, E. R. Brown, J. E. Bjarnason, M. P. Hanson, and A. C. Gossard, "Resonant-optical-cavity photoconductive switch with 0.5% conversion efficiency and 1.0 W peak power," Opt. Lett. **31**(11), 1729–1731 (2006).
10. M. Jarrahi, "Terahertz radiation-band engineering through spatial beam-shaping," IEEE Photonics Technol. Lett. **21**(13), 830–832 (2009).
11. S. Preu, M. Mittendorff, H. Lu, H. B. Weber, S. Winnerl, and A. C. Gossard, "2012 nm ErAs:In(Al)GaAs large area photoconductive emitters," Appl. Phys. Lett. **101**(10), 101105 (2012).
12. S. Preu, G. H. Döhler, S. Malzer, L. J. Wang, and A. C. Gossard, "Tunable, continuous-wave terahertz photomixer sources and applications," J. Appl. Phys. **109**(6), 061301 (2011).
13. M. Bashirpour, M. Forouzmehr, S. E. Hosseininejad, M. Kolahdouz, and M. Neshat, "Improvement of terahertz photoconductive antenna using optical antenna array of ZnO nanorods," Sci. Rep. **9**(1), 1414–1418 (2019).
14. A. Gupta, G. Rana, A. Bhattacharya, A. Singh, R. Jain, R. D. Bapat, S. P. Duttagupta, and S. S. Prabhu, "Enhanced optical-to-THz conversion efficiency of photoconductive antenna using dielectric nano-layer encapsulation," APL Photonics **3**(5), 051706 (2018).
15. M. Bashirpour, J. Poursafar, M. Kolahdouz, M. Hajari, M. Forouzmehr, M. Neshat, H. Hajihoseini, M. Fathipour, Z. Kolahdouz, and G. Zhang, "Terahertz radiation enhancement in dipole photoconductive antenna on LT-GaAs using a gold plasmonic nanodisk array," Opt. Laser Technol. **120**, 105726 (2019).
16. H. Tanoto, J. H. Teng, Q. Y. Wu, M. Sun, Z. N. Chen, S. A. Maier, B. Wang, C. C. Chum, G. Y. Si, A. J. Danner, and S. J. Chua, "Nano-antenna in a photoconductive photomixer for highly efficient continuous wave terahertz emission," Sci. Rep. **3**(1), 2824–2826 (2013).
17. X. Li, N. T. Yardimci, and M. Jarrahi, "A polarization-insensitive plasmonic photoconductive terahertz emitter," AIP Adv. **7**(11), 115113 (2017).
18. M. Khorshidi, S. Zafari, and G. Dadashzadeh, "Increase in terahertz radiation power of plasmonic photoconductive antennas by embedding buried three-stepped rods in electrodes," Opt. Express **27**(16), 22327–22338 (2019).
19. D. V. Lavrukhin, A. E. Yachmenev, I. A. Glinskiy, R. A. Khabibullin, Y. G. Goncharov, M. Ryzhii, T. Otsuji, I. E. Spector, M. Shur, M. Skorobogatiy, and K. I. Zaytsev, "Terahertz photoconductive emitter with dielectric-embedded high-aspect-ratio plasmonic grating for operation with low-power optical pumps," AIP Adv. **9**(1), 015112 (2019).
20. F. Fesharaki, A. Jooshesh, V. Bahrami-Yekta, M. Mahtab, T. Tiedje, T. E. Darcie, and R. Gordon, "Plasmonic antireflection coating for photoconductive terahertz generation," ACS Photonics **4**(6), 1350–1354 (2017).
21. A. Jooshesh, F. Fesharaki, V. Bahrami-Yekta, M. Mahtab, T. Tiedje, T. E. Darcie, and R. Gordon, "Plasmon-enhanced LT-GaAs/AlAs heterostructure photoconductive antennas for sub-bandgap terahertz generation," Opt. Express **25**(18), 22140–22148 (2017).
22. B. Sartorius, H. Roehle, H. Künzel, J. Böttcher, M. Schlak, D. Stanze, H. Venghaus, and M. Schell, "All-fiber terahertz time-domain spectrometer operating at 1.5 µm telecom wavelengths," Opt. Express **16**(13), 9565–9570 (2008).
23. U. Nandi, J. C. Norman, A. C. Gossard, H. Lu, and S. Preu, "2018-nm driven ErAs: In(Al)GaAs photoconductor-based terahertz time domain system with 6.5 THz bandwidth," J. Infrared, Millimeter, Terahertz Waves **39**(4), 340–348 (2018).
24. J. Mangeney, N. Chimot, L. Meignien, N. Zerounian, P. Crozat, K. Blary, J. F. Lampin, and P. Mounaix, "Emission characteristics of ion-irradiated $In_{0.53}Ga_{0.47}As$ based photoconductive antennas excited at 1.55 µm," Opt. Express **15**(14), 8943–8950 (2007).

25. N. Chimot, J. Mangeney, L. Joulaud, P. Crozat, H. Bernas, K. Blary, and J. F. Lampin, "Terahertz radiation from heavy-ion-irradiated $\mathrm{In_{0.53}Ga_{0.47}As}$ photoconductive antenna excited at 1.55 μm," Appl. Phys. Lett. **87**(19), 193510 (2005).
26. J. Mangeney and P. Crozat, "Ion-irradiated $\mathrm{In_{0.53}Ga_{0.47}As}$ photoconductive antennas for THz generation and detection at 1.55 μm wavelength," C. R. Phys. **9**(2), 142–152 (2008).
27. R. J. B. Dietz, M. Gerhard, D. Stanze, M. Koch, B. Sartorius, and M. Schell, "THz generation at 1.55 μm excitation: six-fold increase in THz conversion efficiency by separated photoconductive and trapping regions," Opt. Express **19**(27), 25911–25917 (2011).
28. R. B. Kohlhaas, S. Breuer, L. Liebermeister, S. Nellen, M. Deumer, M. Schell, M. P. Semtsiv, W. T. Masselink, and B. Globisch, "637 μW emitted terahertz power from photoconductive antennas based on rhodium doped InGaAs," Appl. Phys. Lett. **117**(13), 131105 (2020).
29. B. Globisch, R. J. B. Dietz, R. B. Kohlhaas, T. Göbel, M. Schell, D. Alcer, M. Semtsiv, and W. T. Masselink, "Iron doped InGaAs: Competitive THz emitters and detectors fabricated from the same photoconductor," J. Appl. Phys. **121**(5), 053102 (2017).
30. U. Nandi, K. Dutzi, A. Deninger, H. Lu, J. Norman, A. C. Gossard, N. Vieweg, and S. Preu, "ErAs:In(Al)GaAs photoconductor-based time domain system with 4.5 THz single shot bandwidth and emitted terahertz power of 164 μW," Opt. Lett. **45**(10), 2812–2815 (2020).
31. B. Globisch, R. J. B. Dietz, T. Göbel, M. Schell, W. Bohmeyer, R. Müller, and A. Steiger, "Absolute terahertz power measurement of a time-domain spectroscopy system," Opt. Lett. **40**(15), 3544–3547 (2015).
32. A. Mingardi, W. D. Zhang, E. R. Brown, A. D. Feldman, T. E. Harvey, and R. P. Mirin, "High power generation of THz from 1550-nm photoconductive emitters," Opt. Express **26**(11), 14472–14478 (2018).
33. R. J. B. Dietz, B. Globisch, M. Gerhard, A. Velauthapillai, D. Stanze, H. Roehle, M. Koch, T. Göbel, and M. Schell, "64 μW pulsed terahertz emission from growth optimized InGaAs/InAlAs heterostructures with separated photoconductive and trapping regions," Appl. Phys. Lett. **103**(6), 061103 (2013).
34. D. Turan, P. K. Lu, N. T. Yardimci, Z. Liu, L. Luo, J.-M. Park, U. Nandi, J. Wang, S. Preu, and M. Jarrahi, "Wavelength conversion through plasmon-coupled surface states," Nat. Commun. **12**(1), 1–8 (2021).
35. C. W. Berry, N. Wang, M. R. Hashemi, M. Unlu, and M. Jarrahi, "Significant performance enhancement in photoconductive terahertz optoelectronics by incorporating plasmonic contact electrodes," Nat. Commun. **4**(1), 1622–1710 (2013).
36. N. T. Yardimci and M. Jarrahi, "Nanostructure-Enhanced Photoconductive Terahertz Emission and Detection," Small **14**(44), 1802437 (2018).
37. B. Heshmat, H. Pahlevaninezhad, Y. Pang, M. Masnadi-Shirazi, R. B. Lewis, T. Tiedje, R. Gordon, and T. E. Darcie, "Nanoplasmonic terahertz photoconductive switch on GaAs," Nano Lett. **12**(12), 6255–6259 (2012).
38. N. T. Yardimci, H. Lu, and M. Jarrahi, "High power telecommunication-compatible photoconductive terahertz emitters based on plasmonic nano-antenna arrays," Appl. Phys. Lett. **109**(19), 191103 (2016).
39. M. Jarrahi, "Advanced photoconductive terahertz optoelectronics based on nano-antennas and nano-plasmonic light concentrators," IEEE Trans. Terahertz Sci. Technol. **5**(3), 391–397 (2015).
40. C. W. Berry, M. R. Hashemi, and M. Jarrahi, "Generation of high power pulsed terahertz radiation using a plasmonic photoconductive emitter array with logarithmic spiral antennas," Appl. Phys. Lett. **104**(8), 081122 (2014).
41. C. W. Berry and M. Jarrahi, "Terahertz generation using plasmonic photoconductive gratings," New J. Phys. **14**(10), 105029 (2012).
42. B. Y. Hsieh and M. Jarrahi, "Analysis of periodic metallic nano-slits for efficient interaction of terahertz and optical waves at nano-scale dimensions," J. Appl. Phys. **109**(8), 084326 (2011).
43. N. T. Yardimci, S. Cakmakyapan, S. Hemmati, and M. Jarrahi, "A high-power broadband terahertz source enabled by three-dimensional light confinement in a plasmonic nanocavity," Sci. Rep. **7**(1), 1–8 (2017).
44. N. T. Yardimci, R. Salas, E. M. Krivoy, H. P. Nair, S. R. Bank, and M. Jarrahi, "Impact of substrate characteristics on performance of large area plasmonic photoconductive emitters," Opt. Express **23**(25), 32035–32043 (2015).
45. N. T. Yardimci, S. H. Yang, C. W. Berry, and M. Jarrahi, "High-power terahertz generation using large-area plasmonic photoconductive emitters," IEEE Trans. Terahertz Sci. Technol. **5**(2), 223–229 (2015).
46. S. H. Yang, M. R. Hashemi, C. W. Berry, and M. Jarrahi, "7.5% optical-to-terahertz conversion efficiency offered by photoconductive emitters with three-dimensional plasmonic contact electrodes," IEEE Trans. Terahertz Sci. Technol. **4**(5), 575–581 (2014).
47. C. W. Berry, M. R. Hashemi, S. Preu, H. Lu, A. C. Gossard, and M. Jarrahi, "High power terahertz generation using 1550 nm plasmonic photomixers," Appl. Phys. Lett. **105**(1), 011121 (2014).
48. J. Lu, S. H. Lee, X. Li, S. C. Lee, J. H. Han, O. P. Kown, and K. A. Nelson, "Efficient terahertz generation in highly nonlinear organic crystal HMB-TMS," Opt. Express **26**(23), 30786–30794 (2018).
49. A. Rovere, Y. G. Jeong, R. Piccoli, S. H. Lee, S. C. Lee, O. P. Kwon, M. Jazbinsek, R. Morandotti, and L. Razzari, "Generation of high-field terahertz pulses in an HMQ-TMS organic crystal pumped by an ytterbium laser at 1030 nm," Opt. Express **26**(3), 2509–2516 (2018).
50. G. Klatt, B. Surrer, D. Stephan, O. Schubert, M. Fischer, J. Faist, A. Leitenstorfer, R. Huber, and T. Dekorsy, "Photo-Dember terahertz emitter excited with an Er: fiber laser," Appl. Phys. Lett. **98**(2), 021114 (2011).
51. M. L. Smith, R. Mendis, R. E. M. Vickers, and R. A. Lewis, "Comparison of photoexcited p-InAs THz radiation source with conventional thermal radiation sources," J. Appl. Phys. **105**(6), 063109 (2009).

52. T. Seifert, S. Jaiswal, U. Martens, J. Hannegan, L. Braun, P. Maldonado, F. Freimuth, A. Kronenberg, J. Henrizi, I. Radu, and E. Beaurepaire, "Efficient metallic spintronic emitters of ultrabroadband terahertz radiation," Nat. Photonics **10**(7), 483–488 (2016).
53. U. Nandi, M. S. Abdelaziz, S. Jaiswal, G. Jakob, O. Gueckstock, S. M. Rouzegar, T. S. Seifert, M. Kläui, T. Kampfrath, and S. Preu, "Antenna-coupled spintronic terahertz emitters driven by a 1550 nm femtosecond laser oscillator," Appl. Phys. Lett. **115**(2), 022405 (2019).
54. M. A. Haase, V. M. Robbins, N. Tabatabaie, and G. E. Stillman, "Subthreshold electron velocity-field characteristics of GaAs and $In_{0.53}Ga_{0.47}As$," J. Appl. Phys. **57**(6), 2295–2298 (1985).
55. G. Sabatini, C. Palermo, P. Ziade, T. Laurent, H. Marinchio, H. Rodilla, J. Mateos, T. Gonzalez, R. Teissier, and L. Varani, "Monte Carlo study of ballistic effects in high speed InAs-based quantum hot electron transistor," in *35th Int. Conf. Infrared Millim. Terahertz Waves* (2010), pp. 1–2.
56. Y. Taur and T. H. Ning, *Fundamentals of modern VLSI devices*, (Cambridge University, 2013).
57. E. Khutsishvilii, Z. Chubinishvili, G. Kekelidze, I. Kalandadze, T. Qamushadze, and M. Metskhvarishvili, "The Features of Electronic Conduction in InAs," European J. Eng. Technol. Research **6**(3), 10–13 (2021).
58. E. S. Harmon, M. L. Lovejoy, M. R. Melloch, M. S. Lundstrom, D. Ritter, and R. A. Hamm, "Minority-carrier mobility enhancement in p+ InGaAs lattice matched to InP," Appl. Phys. Lett. **63**(5), 636–638 (1993).
59. H. Arabshahi, M. R. Khalvati, and M. Rezaee Rokn-Abadi, "Temperature and doping dependencies of electron mobility in InAs, AlAs and AlGaAs at high electric field application," Brazilian J. Phys. **38**(3a), 293–296 (2008).
60. K. Brennan, "Theory of the steady-state hole drift velocity in InGaAs," Appl. Phys. Lett. **51**(13), 995–997 (1987).
61. F. P. Kesamanly, Y. MaTtsev, D. N. Nasledov, L. A. Nikolaeva, M. N. Pivovarov, V. A. Skripkin, and Y. I. Uvanov, "Structure of the conduction band in indium arsenide (Indium arsenide crystals conduction band structure with various electron concentrations, determining electron mass dependence on concentration and temperature)," Fiz. Tekhn. Polupr. **3**(8), 1182–1187 (1969).
62. T. P. Pearsall, *GaInAsP Alloy Semiconductors*, (John Wiley and Sons, 1982).
63. I. Tångring, Y. X. Song, Z. H. Lai, S. M. Wang, M. Sadeghi, and A. Larsson, "A study of the doping influence on strain relaxation of graded composition InGaAs layers grown by molecular beam epitaxy," J. Crystal Growth **311**(7), 1684–1687 (2009).
64. K. E. Lee and E. A. Fitzgerald, "High-quality metamorphic compositionally graded InGaAs buffers," J. Crystal Growth **312**(2), 250–257 (2010).
65. P. Kidd, D. J. Dunstan, H. G. Colson, M. A. Louren, A. Sacedo, F. Gonza, L. Gonza, Y. Gonza, R. Garci, D. Gonza, and F. J. Pacheco, "Comparison of the crystalline quality of step-graded and continuously graded InGaAs buffer layers," J. Crystal Growth **169**(4), 649–659 (1996).
66. S. Kalem, J. I. Chyi, H. Morkoç, R. Bean, and K. Zanio, "Growth and transport properties of InAs epilayers on GaAs," Appl. Phys. Lett. **53**(17), 1647–1649 (1988).
67. S. M. Sze, Y. Li, and K. K. Ng, *Physics of Semiconductor Devices*, (Wiley, 2021).
68. S. L. Teitel and J. W. Wilkins, "Ballistic transport and velocity overshoot in semiconductors: Part I—Uniform field effects," IEEE Trans. Electron Devices **30**(2), 150–153 (1983).
69. G. H. Döhler, F. Renner, O. Klar, M. Eckardt, A. Schwanhäußer, S. Malzer, D. Driscoll, M. Hanson, A. C. Gossard, G. Loata, and T. Löffler, "THz-photomixer based on quasi-ballistic transport," Semiconductor Sci. Technol. **20**(7), S178–S190 (2005).
70. K. Brennan and K. Hess, "High field transport in GaAs, InP and InAs," Solid-State Electron. **27**(4), 347–357 (1984).
71. J. Park, J. H. Kang, X. Liu, S. J. Maddox, K. Tang, P. C. McIntyre, S. R. Bank, and M. L. Brongersma, "Dynamic thermal emission control with InAs-based plasmonic metasurfaces," Sci. Adv. **4**(12), 3163 (2018).